Comparing ASM and Learning-Based Methods for Satellite Image Dehazing

Steven Christ Pinantyo Arwidarasto¹, Laksmita Rahadianti¹

¹ Faculty of Computer Science, University of Indonesia, Depok 16424, Indonesia

Email:steven.christ31@ui.ac.id

Abstract

Recent advancements in optical satellite technologies have significantly improved image resolution, providing more detailed information about Earth's surface. However, atmospheric interference, such as haze, is still a major factor in image capture. The interference results in visibility degradation of the acquired images, hindering computer vision tasks. Numerous studies have proposed various methods to recover haze-affected regions in satellite images, highlighting the need for more effective solutions. Motivated by this, this paper compares different atmospheric dehazing methods, including Atmospheric Scattering Model (ASM)-based and deep learning-based. The results show that SRD is the best ASM-based method, with a PSNR value of 19.09 dB and an SSIM of 0.908. Among deep learning models, DW-GAN achieves the best restoration results with a PSNR value of 26.22 dB and an SSIM of 0.959. SRD offers faster inference times, but still suffers from residual haze and noticeable color degradation compared to DW-GAN. In contrast, DW-GAN provides a more complete haze removal at the cost of higher computational demands than ASM-based methods.

Keywords: satellite, scattering, dehazing, prior, deep learning

1. Introduction

The advancement of optical satellite technology has enabled the acquisition of more detailed images of the Earth's surface for various computer vision applications. Some examples are land cover mapping [1] for urban planning, change detection for abrasion monitoring [2, 3], and classification of plant diseases [4]. However, optical satellite imagery still suffers from degradation caused by atmospheric conditions, such as haze. These conditions occur due to dispersed particles larger than air molecules but smaller than fog in the air due to changes in relative humidity in the atmosphere [5, 6]. These particles affect traveling light rays [7], which undergo reflection, refraction, and absorption as they pass through the atmosphere [8]. This results in a reduced light intensity transmitted to the Earth's surface and reflected to the satellite's optics, contributing to a decline in object visibility in the final acquired image. This low visibility negatively impacts computer vision tasks that require clear object structures, colors, and textures, leading to errors such as incorrect classification in land cover mapping [9].

The simplest solution involves retaking the image under clear conditions at a different time. However, this comes at the expense of more resources and time to ensure high-quality image acquisition. Alternatively, many works have been proposed to restore images from haze, which is also commonly known as dehazing. These techniques are based on the atmospheric scattering model (ASM) [5, 10–12], which provides a simplified mathematical equation that models the scattering of light traveling through a medium [6]. In mathematical terms, this model can be written in Equation (1).

$$I(x) = J(x)t(x) + A(1 - t(x))$$
(1)

where I(x) represents the degraded image, J(x) represents the undegraded image, t(x) describes the transmission mapping, and A describes the global atmospheric light or the ambient light in the atmosphere.

The ASM model consists of two crucial calculations. The first is the J(x)t(x) term, which calculates the direct attenuation that describes the

decay of light when traversing the medium to the sensor. The second is A(1-t(x)), which describes the phenomenon in which the atmosphere itself acts as a light source [6] causing a change in colors [13] and disrupting the original path of light. Therefore, to obtain the restored image, Equation (1) can be adapted as Equation (2), with 0.1 as the lower bound of transmission to prevent division by zero.

$$J(x) = \frac{I(x) - A}{\min(0.1, t(x))} + A \tag{2}$$

Solving the ASM for image restoration requires three known essential variables: the haze-affected image I, atmospheric light values A, and transmission t(x). However, in a single-image haze restoration task, A and t(x) are unknown, adding to the image restoration challenge. He et al., [10] proposed the Dark Channel Prior (DCP) to estimate A and t(x) through the image's dark pixels. However, DCP [10] fails in the presence of white-colored, nonsky objects, which can be detected as haze. Hence, Jackson et al., [11] proposed a hybrid method to reduce the influence of white-colored objects by combining the brightest pixel acquisition, namely Bright Channel Prior (BCP) and DCP. However, neither technique accounts for the non-homogeneous nature of haze in satellite images.

To address satellite images specifically, He et al., [12] introduced Superpixel Remote Sensing Dehazing (SRD) by incorporating superpixel clustering. Unlike other ASM-based methods, SRD [12] estimates the transmission map by taking the minimum value from the lowest pixel in each RGB color channel, ensuring non-homogeneous channel-wise transmission values. Despite better performance in haze restoration, estimating atmospheric light and transmission variables remains a complex challenge, especially in highly thick-distributed haze conditions [14].

In recent years, deep learning breakthroughs have introduced promising alternatives for haze removal. Fu et al. [14] proposed a dual-branch network consisting of a prior knowledge branch using Res2Net [15] and a Discrete Wavelet Transform (DWT) branch to solve limited data for training and preservation of details. Zhou et al., [16] followed by incorporating the DWT branch with Fast Fourier Convolution (FFC), contributing to the enlargement of receptive fields. In addition, Zhou et al., [16] replaced the pre-trained Res2Net [15] with ConvNeXt [17] as one of the state-of-the-art network CNN-based architectures, giving high-quality restoration results compared to ASM-based approaches. However, as He et al., [5] pointed out, deep learning-

based methods require sufficient hardware capability and training data to achieve satisfactory results.

Thus, any computer vision application will face the balancing act between restoration performance and computational costs for dehazing. This motivates us to study the latest ASM and DL approaches. The various methods are then evaluated through a series of benchmarked experiments. This research provides a comparative analysis and discussion of dehazing results using ASM-based and deep-learning-based approaches for satellite images. Through this comparison, it is possible to find the most efficient and accurate approach for satellite image dehazing as needed.

2. Materials

In this study, we devise experiments to compare and analyze various dehazing methods. We compare 4 ASM-based methods, i.e., DCP [10], BDCP [11], HALP [5], and SRD [12]; as well as 2 deep learning methods, i.e., DW-GAN [14], and DWT-FFC [16]. The dehazing is conducted on a benchmarked synthetic haze dataset, and the results are evaluated using the same evaluation metrics. Both types of methods have strengths and weaknesses when applied in satellite image dehazing scenarios.

2.1. Dark Channel Prior (DCP)

He et al., [10] introduced Dark Channel Prior (DCP) as atmospheric light and transmission values estimation that built on the assumption that in the natural image, the shadow of objects contributes to at least one low-pixel intensity colored channel. The low pixel intensity results from several factors, such as object shadows, colored objects, and dark-colored surfaces. He et al., [10] observed that haze-affected regions seem brighter due to high-intensity pixels, which can be used to detect haze-affected areas.

DCP [10] begins by patching the image into several segments or patches, from which the lowest RGB pixel will be extracted. The dark pixels mapping undergoes sorting to extract the top 0.1% brightest pixels from the dark pixels mapping as global atmospheric light estimation. The obtained atmospheric light values will be used to estimate transmission mapping by channel-wise dividing the hazy image and the atmospheric light values. Finally, the estimated atmospheric and transmission values will be used to restore the haze-free image using Equation (2). The transmission estimation module can work as such due to dark prior, where the unaffected region will have near-zero dark mapping values.

2.2. Bright Channel and Dark Channel Prior (BDCP)

The Dark Channel Prior (DCP) [10] has limitations regarding white objects, such as sky regions, which lack low-intensity pixels. To address this, Jackson et al., [11] proposed the combination of Dark Prior and Bright Prior (BDCP), integrating Bright and Dark Channel Prior for more accurate atmospheric light and transmission mapping. Additionally, BDCP uses a guided Filter to replace soft matting in DCP [10] to reduce computational overhead. BDCP estimates atmospheric light by patching, from which the top 0.1% minimum and maximum channel pixels are extracted from the bright and dark pixels mapping, respectively. The darkest pixels from bright pixels mapping will balance the influence of high-intensity pixels of white objects from dark pixels mapping, contributing to more accurate atmospheric light estimation and transmission mapping.

2.3. Heterogeneous Atmospheric Light Prior (HALP)

Most ASM-based methods, such as DCP [10] and BDCP [11], focus more on restoring natural scenery, not remote sensing imagery. Due to the very long near-vertical distance [5] between the satellite and the Earth's surface, the depth values are considered uniform across the image for satellite images [12], unlike natural scenes, where the image visibility is tied to the horizontal distance. The long near-vertical distance also contributes to the degradation of transmitted light [18, 19], affecting visibility. In addition, the broad spatial coverage information retrieval ability of remote sensing introduces non-uniform haze distribution.

He et al., [5] addressed the non-uniform nature of haze in remote sensing by introducing Heterogeneous Atmospheric Light Estimation (HALP), which employs a patch-based module for atmospheric light estimation. This method obtains local atmospheric light values using the HSV color space and a square patching strategy to divide the image into several local regions. Then, the maximum V component is extracted from each local region, which is then used to obtain the haze-affected region. In addition. HALP considers the issue of box filters that cover irrelevant image regions by incorporating a Side Window Filter (SWF) to estimate and refine transmission from dark pixel mapping. SWF works by convoluting eight different filters that fit the edges of the image.

2.4. Superpixel Remote Sensing Dehazing (SRD)

Despite the heterogeneous nature provided by the modified ASM through the patch-based module [5], the square patching strategy introduces a new issue in defining the optimum patch size that can accurately represent the atmospheric light estimation on a particular region. In addition, HALP [5] does not consider the heterogeneous wavelength degradation effect by particles in the atmosphere. To address these issues, He et al., [12] introduced Superpixel Remote Sensing Dehazing (SRD), which incorporates superpixel modules as a replacement for the square patching strategy, giving the method the ability to extract pixel representation based on the area with the same characteristics such as color. structure, luminance, and contrast. Additionally, the transmission estimation is no longer obtained from division operation but through performing dark pixel mapping on each RGB channel, ensuring nonhomogeneous channel-wise transmission values.

2.5. Discrete Wavelet-Generative Adversarial Network (DW-GAN)

In general, ASM-based methods lack the ability to eliminate the presence of haze and do not work well under dense haze conditions. Deep learning approaches, particularly Convolution Neural Networks (CNNs), excel in reconstructing objects affected by the thick haze close to their ground truth in an endto-end manner. Fu et al., [14] proposed a dual-branch network called the Discrete Wavelet Generative Adversarial Network (DW-GAN). The first branch is called prior-knowledge, a U-Net architecture that uses pre-trained Res2Net [15] to mitigate data limitation issues and promote multiscale feature extraction by leveraging previously learned feature maps that create a combination effect. Finally, the prior knowledge network is also integrated with Channel-Pixel-wise Attention [20], allowing the model to adapt to the nature of heterogeneous haze distribution

Meanwhile, the second branch features the Discrete Wavelet (DW) branch with U-Net-like architecture integrated with Haar Wavelet Transform, which decomposes images through high-pass and low-pass filtered feature maps [14]. During the training phase, the model uses a Generative Adversarial Network (GAN) schema, ensuring sharp details through adversarial loss that utilizes a Discriminator to classify whether the generated image is close to the ground truth or otherwise. On the other hand, DW-GAN

architecture will act as a Generator to reconstruct the haze-free images.

2.6. Discrete Wavelet Transform-Fast Fourier Convolution (DWT-FFC)

Zhou et al., [16] introduced Discrete Wavelet Transform-Fast Fourier Convolution (DWT-FFC), which consists of dual-branch networks inspired by DW-GAN [14] with the integration of Fast Fourier Convolution (FFC) [21] in the bottleneck layers. The integration of FFC and DWT enables the model to learn the spatial and frequency information of the affected haze region. Following the Fourier theory, where a change in one frequency will alter the rest of the spatial points [21], this enhances the receptive fields

The FFC scheme consists of a local branch and a global branch, where a spatial residual connection from the local branch complements the information in the global branch that learns information in the frequency domain. DWT-FFC [16] also replaces the existing Res2Net [15] with ConvNeXt [17] for a pre-trained encoder backbone in the prior-knowledge branch to leverage the most state-of-the-art CNN model that achieved outstanding evaluation metrics in several classification tasks [17]. Similar to DW-GAN [14], DWT-FFC [16] is trained using a Generative Adversarial Network (GAN) scheme.

3. Methods

This study conducted satellite image dehazing using 6 methods, consisting of 4 ASM-based methods, i.e., DCP [10], BDCP [11], HALP [5], and SRD [12]; as well as 2 deep learning methods, i.e., DW-GAN [14] and DWT-FFC [16]. The experiment design is shown in Figure 1. The experiment flow consists of dataset acquisition, pre-processing, training, validation (for deep learning-based methods only), inference or testing, and evaluation.

The deep learning methods will separate the dataset into training, validation, and testing sets for each phase, which are then trained using the NVIDIA DGX-A100 GPU. Meanwhile, the ASM-based methods will use the testing set only, as they do not require a training phase. We also tune several parameters and implement image pre-processing to adapt to the original model configuration's input dimensions.

During the testing phase of both the ASM-based and deep learning models, inference is done on an Intel Xeon 2.20 GHz CPU. After inference, we compare the restored results of each method using full-reference image quality evaluation metrics. Finally,

Table 1. Parameter configuration for deep learning approaches.

| oution. | | |
|----------------|---------------|---------------|
| Parameters | DW-GAN [14] | DWT-FFC [16] |
| Epochs | 1,000 | 1,000 |
| Optimizer | Adam | Adam |
| Learning Rate | 0.0001 | 0.0001 |
| Scheduler | Multistep 0.5 | Multistep 0.5 |
| α | 0.2 | 0.2 |
| β | 0.001 | 0.01 |
| $\dot{\gamma}$ | 0.005 | 0.0005 |
| | | |

we provide an analysis of the complexity of the deep learning models and inference time calculation for every method to restore one hazy image.

In this research, we used the Gaofen Satellite 2 (GF-2) SateHaze1k dataset [22], which consists of separate directories representing each thin, medium, and thick haze category. Each category contains 400 images, with 320 images for training, 35 for validation, and 45 for testing.

The images in the SateHaze1k [22] dataset were originally 512×512 pixels, but we resized the images to 256×256 pixels due to resource limitations. We used horizontal flip and random rotation augmentation strategies for the training phase only to create variation in the training dataset for non-equivariant transformation [23]. We apply normalization to convert the image pixels from [0,255] to [-1,1] for the training, validation, and testing phases, as shown in Figure 1.

Regarding the training parameters of deep learning-based methods, hyperparameter tuning was done on the epochs parameter and batch size to address the insufficient availability of resources for training. We use batch size 16 for training, as prescribed by the original author, and an epoch of 1000, which we reduced from the original 10000 epochs. The summary of the training configuration for our deep learning methods is represented in Table 1.

To evaluate the results, we used several metrics to evaluate each method's haze restoration quality. We first use the Peak Signal-to-Noise Ratio (PSNR) to measure the performance of compressed distorted image reconstruction [24]. This metric is based on the Mean Squared Error (MSE) integrated with the signal conversion formula in decibels (dB) as shown in Equation (3), where x and y represent the ground truth and restored hazy image, and MAX represents the maximum pixel value allowed by the image.

$$PSNR(x,y) = 10log_{10} \frac{MAX^2}{MSE(x,y)}$$
 (3)

We also use the Structural Similarity Index (SSIM), which considers the image's structure, lu-

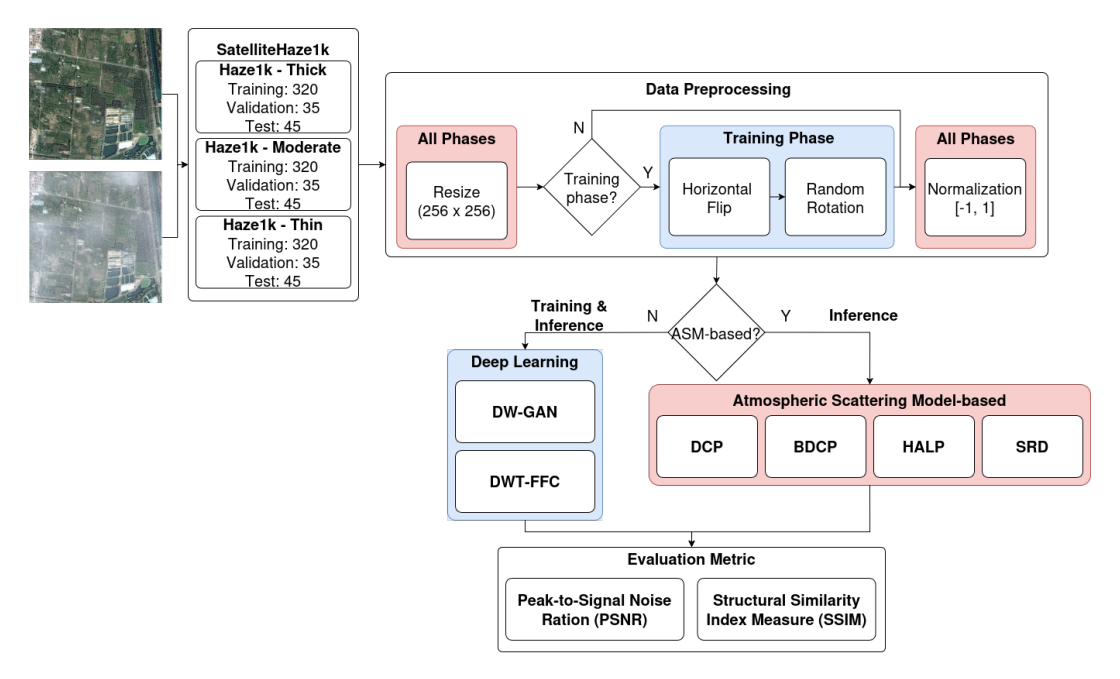


Figure 1. Experiment design on exploring deep learning-based and ASM-based image dehazing approaches.

minance, and contrast aspect [25]. The SSIM computes the final SSIM score by taking the average luminance of the image μ , the standard deviation of image contrast σ , and a constant C to compute the final SSIM score, as in Equation (4).

$$SSIM(x,y) = \frac{(2\mu_x \mu_y + C_1)(2\sigma_x y + C_2)}{(\mu_x^2 + \mu_y^2 + C_1)(\sigma_x^2 + \sigma_y^2 + C_2)}$$
(4)

4. Results and Discussion

This section describes the results obtained for image dehazing on the 6 methods compared in our experiments. We also followed up on the results with a discussion and comparative analysis for each method. We use evaluation metrics for the dehazing results, complexity measures, and inference time to analyze computation requirements.

4.1. Results

The dehazing results of our experiments are shown in Table 2. As we can see, the restoration quality decreases as the haze's thickness increases. This indicates that the ASM-based methods struggle more to restore image regions affected by dense haze. For example, DCP achieves a PSNR/S-SIM score of 14.79/0.818 for thick haze, significantly lower than under medium and thin haze

conditions. The BDCP achieved PSNR/SSIM scores of 20.66/0.933 under thin haze, 20.54/0.925 under medium haze, and 15.11/0.824 under thick haze conditions, with an overall improvement of 1.57% from the DCP results.

Meanwhile, HALP shows unsatisfactory results for all haze thicknesses with an overall PSNR/S-SIM score of 15.88/0.810, likely due to a poorly defined patch size. As described in Section 2.4, the patch size is the method's parameter for extracting local atmospheric light. Different images will require different patch sizes, making fine-tuning harder. Finally, SRD obtains the highest PSNR/SSIM score amongst all ASM-based methods, with a score of 19.09/0.908.

Table 2 also shows that the deep learning-based models perform better in removing the haze, represented by an average PSNR/SSIM score of up to 25/0.952. However, unlike ASM-based methods, the experiments on deep learning-based methods show a pattern in which trained models perform best under medium-haze conditions, followed by thin and thick haze conditions. We suspect that medium-haze patterns get higher evaluation because medium-haze tends to have limited variation in haze thickness than thin haze conditions, which helps the model to focus more on restoring the haze-affected region instead of weighting which region required more haze suppression. In addition, SateHaze1k's moderate thickness resembles thin haze conditions,

| Table 2. Comparison of ASM-based and Deep Learning-based Methods on Combine SateHaze1k training |
|--|
|--|

| Methods | MACs | Inference Time | Th | in | Med | ium | Th | ick | Ave | rage |
|-------------|------|----------------|-------|-------|-------|-------|-------|-------|-------|-------|
| | | | PSNR | SSIM | PSNR | SSIM | PSNR | SSIM | PSNR | SSIM |
| DCP[10] | N/A | 19.80 | 20.26 | 0.932 | 20.39 | 0.926 | 14.79 | 0.818 | 18.48 | 0.892 |
| BDCP[11] | N/A | 0.107 | 20.66 | 0.933 | 20.54 | 0.925 | 15.11 | 0.824 | 18.77 | 0.894 |
| HALP[5] | N/A | 2.495 | 18.62 | 0.891 | 17.08 | 0.865 | 11.56 | 0.710 | 15.88 | 0.810 |
| SRD[12] | N/A | 0.154 | 21.11 | 0.941 | 19.64 | 0.934 | 16.51 | 0.876 | 19.09 | 0.908 |
| DW-GAN[14] | 30.1 | 0.715 | 25.66 | 0.969 | 29.55 | 0.973 | 23.46 | 0.934 | 26.22 | 0.959 |
| DWT-FFC[16] | 90.1 | 4.669 | 25.22 | 0.962 | 27.45 | 0.969 | 23.37 | 0.926 | 25.35 | 0.952 |

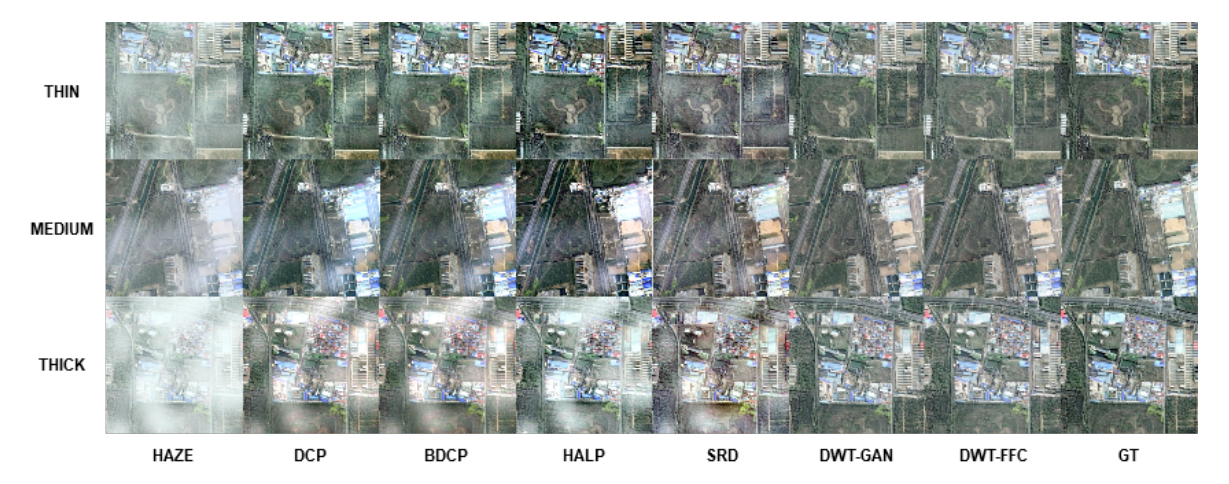


Figure 2. SateHaze1k Restoration Result on DCP [10], BDCP [11], HALP [5], SRD [12], DW-GAN [14] and DWT-FFC [16]

allowing the model to extract as much information as possible to reconstruct a clear image, unlike thick haze conditions where colors and object visibility nearly degrade fully, limiting the ability to reconstruct objects accurately.

Regarding the performance of deep learning models, DW-GAN outperforms DWT-FFC in recovering the image with an average PSNR/SSIM score of 26.22/0.959 compared to DWT-FFC's score of 25.35/0.952. DW-GAN outperforms the image restoration quality of DWT-FFC in all haze thicknesses with slightly higher perceptual quality with PSNR/SSIM scores of 25.66/0.969 under thin haze, 29.55/0.973 under moderate haze, and 23.46/0.934 under thick haze conditions. In addition, in the restoration quality aspect, deep-learning-based methods outperform ASM-based in all of SateHaze1k's thickness benchmark datasets, highlighting the advantages of an end-to-end learning scheme over the ASM-based estimation methods.

The dehazing results of each method are displayed in Figure 2. Through observation, we can confirm that all ASM-based methods struggle to retrieve information degraded by thick haze. This is due to the non-zero transmission of light mapping values to prevent division by zero during the image

restoration calculation. Additionally, the ASM-based methods show signs of over-saturation, visualized by color degradation in unaffected regions that become darker in shades compared to the ground truth one, as well as the appearance of yellowish objects.

Among the ASM-based methods, SRD is superior in significantly reducing haze with non-homogeneous atmospheric light alongside superpixel clustering. However, it is not immune to oversaturation, as represented by several degraded color components. In contrast, DW-GAN and DWT-FFC successfully remove the haze with minimal color degradation, represented by a slightly brighter scene than the ground truth.

Next, we discuss the complexity of the deep learning models. As shown in Table 2, DW-GAN has 51.508M total parameters, while DWT-FFC has 260.270M. Both models' multiplication and addition operations show that DWT-FFC is heavier in terms of memory consumption than DW-GAN with multiply-accumulate operations (MACs) values of 90.1G and 30.1G, respectively. We conclude that DWT-FFC requires more computation power than DW-GAN due to the use of Res2Net and ConvNeXt to deal with limited labeled training data. We identified that the ConvNeXt pre-trained con-

tributed 99% to the total parameters of the DWT-FFC with 260.057M parameters. Likewise, Res2Net contributes 97.3% to the total parameters of DW-GAN with 50.117M. Both methods try to solve the issue of limited training data with pre-trained at the expense of high computation resources.

Finally, we also analyze the inference time needed to restore a single image. As described in Section 3, inference using both the ASM-based and deep learning models is done on Intel Xeon 2.20 GHz CPU. We can see in Table 2 that DCP requires significantly more time to compute as it utilizes a soft matting algorithm to mitigate the block effect caused by the square patching strategy in transmission estimation. In contrast, other ASM-based methods, like BDCP and SRD, leverage the (Fast) Guided Filter, eliminating the additional computational overhead. Similarly, HALP utilizes a Side Window Filter (SWF), contributing to increased computational time, although it remains faster than the soft matting algorithm used by DCP.

Compared to previous methods, DW-GAN has an inference time of 0.715 seconds. While this is longer than BDCP and SRD, it is still faster than DCP and HALP. In contrast, DWT-FFC only outperforms DCP with an inference time of 4.669 seconds, underlining the significant impact of the soft-matting algorithm on the restoration inference time.

The extended inference times of DW-GAN and DWT-FFC are primarily due to the use of pre-trained models: Res2Net in DW-GAN and ConvNext in DWT-FFC, both of which introduce additional complexity. Furthermore, DWT-FFC uses a fast Fourier transform to learn frequency information through standard spatial convolution, which does not take advantage of faster inference following the Fourier theory.

4.2. Discussion

Based on Table 2, the overall results show that deep learning methods perform better than ASM-based methods. The best performing ASM-based model, SRD [12], still falls behind the deep-learning models, proving the limitations of using ASM in the quality restoration of images. This is due to the dependency of estimation accuracy for solving the ASM equation. Deep learning-based methods leverage end-to-end learning, which can consider random factors previously unknown in the defined equation.

Non-Homogeneous Variables in ASM-based Methods. The patching strategy (square/superpixel) used in the ASM-based models is proven to preserve spatial information, providing clear contrast to the

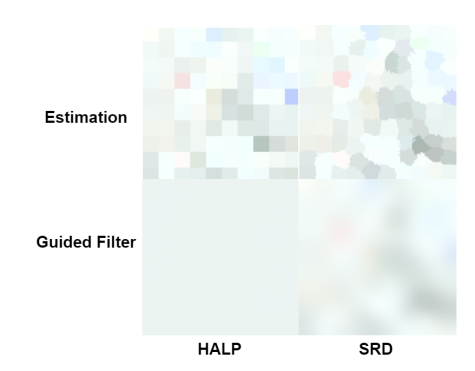


Figure 3. Heterogeneous Atmospheric Light Illustration Estimated by HALP [5] and SRD [12]

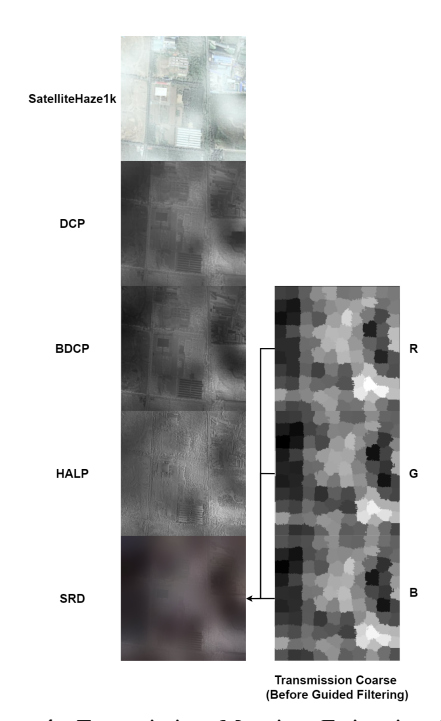


Figure 4. Transmission Mapping Estimation Through DCP [10], BDCP [11], HALP [5], and SRD [12]

pattern of unaffected and haze-affected areas. This evidence is represented in Figure 3 where darker regions in the refined atmospheric light estimation represent non-haze-affected areas. In contrast, white areas represented haze-affected areas where severe light scattering processes occur.

Despite preserving structural information, the optimal patch size is a hyperparameter that must be selected carefully for accurate and representative local atmospheric light estimation. Figure 3 shows that square patching struggles to maintain the contrast between haze-covered and clear areas due to large patch sizes. This is a significant drawback

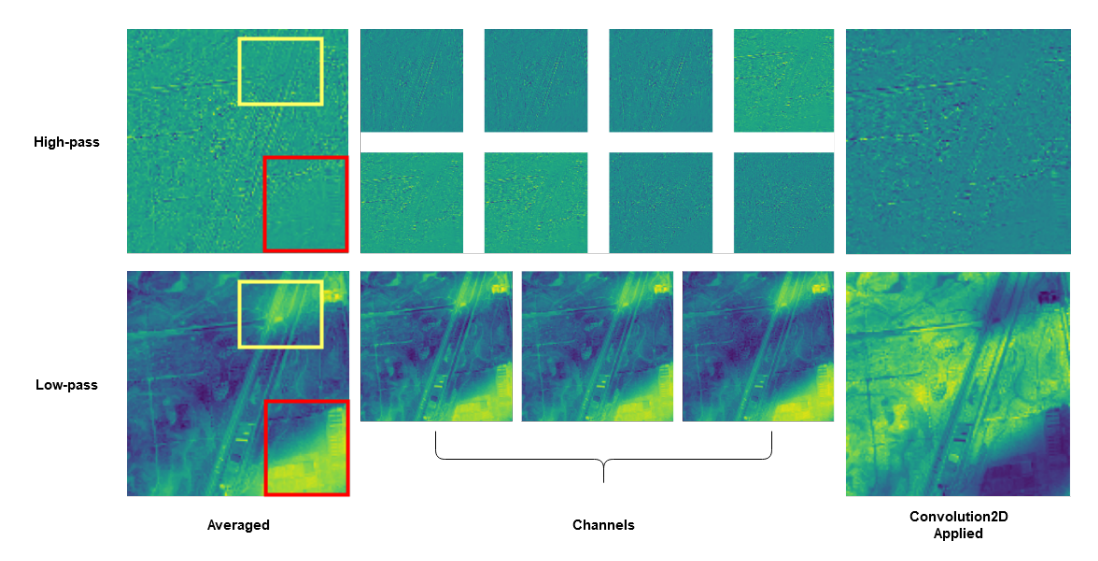


Figure 5. Discrete Wavelet Transform

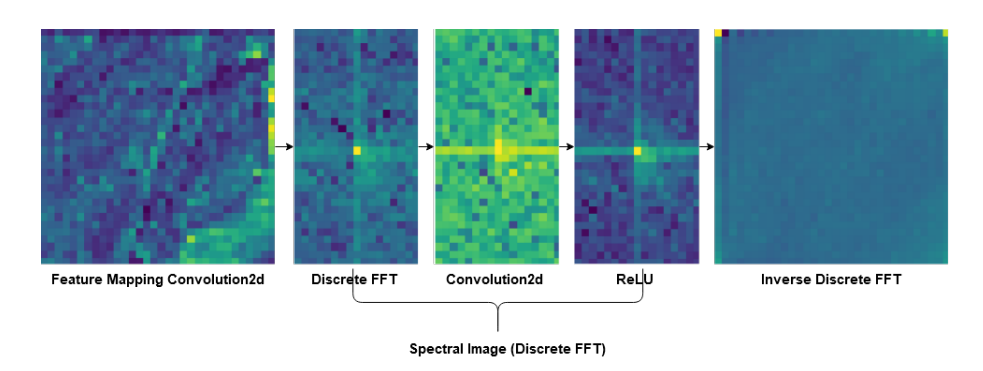


Figure 6. Convolution on Spectral Domain

of using a square patching module. The diverse haze distribution pattern and thickness also demand a non-uniform patch size definition for every image. In contrast, superpixel patching is superior in capturing haze-affected regions, proven by visible haze patterns due to clustered objects with similar characteristics. Even if superpixel patching still encounters the patch size issue, it compensates with the clustering process.

Figure 4 shows the transmission map estimation results of the ASM-based models. Compared to non-homogeneous channel-wise transmission, integrating BCP with DCP provides a decent alternative to enhance the contrast of the disrupted light transmission by reducing the influence of white objects. Therefore, the generated transmission tends to have a darker shade for the severe haze effect and a lighter shade for the less affected region represented in the transmission mapping.

The SWF module in HALP provides an alternative for transmission estimation through convolution to reduce image grid effects created by square patching. It preserves the haze-affected region yet is pale, as shown by the lighter shade of the hazeaffected area, which describes the significance of the haze-affected region. In contrast to other ASMbased methods, SRD [12] obtains the transmission by solely using superpixel patching and dark pixels through each color channel without requiring division operation of the haze and atmospheric light images. Bolstered with superpixel clustering, SRD [12] can obtain characteristics-specific transmission values where severe haze thickness resides, making it easier to detect visualized by darker shade than other DCP-based methods.

Discrete Wavelet Transform (DWT). With the conversion of the spatial domain to the frequency domain through Haar Discrete Wavelet, as presented

in Figure (5), the feature map will undergo a decomposition process that produces a low-pass-filtered image (LL) and high-pass-filtered images (LH, HL, HH). The high-pass-filtered feature maps highlight details in light haze-affected regions, visualized by texture patterns. These patterns can help the decoder improve its ability to reconstruct crisp details. In contrast, the low-level features will produce a downsampled image, which is fused along the previous convolution layers to the following encoder layers, providing more context information for feature extraction. Figure (5) shows that the DWT module can preserve details, such as roads, which we highlight with a yellow box. However, extracting line patterns from densely haze-affected regions still poses a challenge, as shown by the high-pass filtered image represented by the area inside the red box.

Fourier Transform. Fast Fourier Convolution (FFC) leverages the Fourier theory, which allows capturing a broader context, enabling us to perform a 1×1 convolution operation on the Fourier spectrum. This operation will alter the spatial information context and facilitate global context extraction to estimate the haze-affected pixel. Figure 6 illustrates the FFC result, in which the convolution performed in the frequency domain produces feature maps with soft structural details, suppressing high-frequency to reduce noise levels as well as reducing texture that will be added from the local convolution branch.

5. Conclusion

We successfully conducted dehazing experiments on satellite images using the synthetic Sate-Hazelk dataset. We compared 6 dehazing methods, consisting of 4 ASM-based methods, i.e., DCP [10], BDCP [11], HALP [5], and SRD [12]; as well as 2 deep learning methods, i.e., DW-GAN [14], and DWT-FFC [16]. Overall, deep learning-based methods provide higher restoration quality at the expense of high computational power. The best performing deep learning method was DW-GAN, with a PSNR/SSIM score of 26.22/0.959, outperforming DWT-FFC in both restoration quality and complexity. Although it still left some color degradation, this method effectively removed haze layers in an image. Meanwhile, ASM-based methods excel in providing haze reduction with low computational power. The best-performing ASM-based model, SRD, offers significant haze reduction, with an overall PSNR/SSIM score of 19.09/0.908. Additionally, SRD provides a faster inference time than the other ASM-based models, making it suitable for reducing the haze effect in non-dense haze conditions.

Acknowledgement

The authors express gratitude to the UI AI Center of Excellence, Faculty of Computer Science, Universitas Indonesia, for providing access to the NVIDIA DGX-A100 system necessary to run the experiments.

References

- [1] S. Liu, H. Wang, Y. Hu, M. Zhang, Y. Zhu, Z. Wang, D. Li, M. Yang, and F. Wang, "Land use and land cover mapping in china using multimodal fine-grained dual network," *IEEE Transactions on Geoscience and Remote Sensing*, vol. 61, pp. 1–19, 2023.
- [2] I. G. W. S. Dharma and A. M. Arymurthy, "Shoreline change detection based on multispectral images using 2d-principal component analysis of band images and histogram of oriented gradient features," in 2017 International Conference on Advanced Computer Science and Information Systems (ICACSIS), 2017, pp. 315–320.
- [3] B. T. Rumahorbo, M. Warpur, and B. Hamuna, "Detection of shoreline changes due to abrasion and accretion using landsat imagery—a case study in the coastal areas of supiori regency, indonesia," *Ecological Engineering & Environmental Technology*, vol. 24, 2023.
- [4] A. C. Ramachandra, N. Rajesh, K. Aishwarya, N. Madugonda, R. A. Akash, and G. Namratha, "Classification of crop diseases through remote-sensed data using multi-class svm," in 2022 IEEE 2nd Mysore Sub Section International Conference (MysuruCon), 2022, pp. 1–5
- [5] Y. He, C. Li, and X. Li, "Remote sensing image dehazing using heterogeneous atmospheric light prior," *IEEE Access*, vol. 11, pp. 18805–18820, 2023.
- [6] S. G. Narasimhan and S. K. Nayar, "Vision and the atmosphere," *International Journal of Computer Vision*, vol. 48, pp. 233–254, 07 2002.
- [7] S. Agrawal and G. B. Khairnar, "A comparative assessment of remote sensing imaging techniques: Optical, sar and lidar," *The International Archives of the Photogrammetry, Remote Sensing and Spatial Information Sciences*, vol. XLII-5/W3, pp. 1–6, 2019.
- [8] M. A. Reddy, *Textbook of Remote Sensing and Geographical Information Systems*, 3rd ed. BS Publications, 2008.
- [9] L. Han, Y. Zhao, H. Lv, Y. Zhang, H. Liu, and G. Bi, "Remote sensing image denoising

- based on deep and shallow feature fusion and attention mechanism," *Remote Sensing*, vol. 14, no. 5, 2022.
- [10] K. He, J. Sun, and X. Tang, "Single image haze removal using dark channel prior," in 2009 IEEE Conference on Computer Vision and Pattern Recognition, 2009, pp. 1956–1963.
- [11] J. Jackson, O. Ariyo, K. Acheampong, M. Boakye, E. Frimpong, E. Ashalley, and Y. Rao, "Hybrid single image dehazing with bright channel and dark channel priors," in 2017 2nd International Conference on Image, Vision and Computing (ICIVC), 2017, pp. 381– 385.
- [12] Y. He, C. Li, and T. Bai, "Remote sensing image haze removal based on superpixel," *Remote Sensing*, vol. 15, no. 19, 2023.
- [13] J. R. Panicker, M. Student, and A. Professor, "Review on dehazing based on atmospheric scattering model," *International Journal of Creative Research Thoughts*, vol. 6, pp. 2320–2882, 2018.
- [14] M. Fu, H. Liu, Y. Yu, J. Chen, and K. Wang, "Dw-gan: A discrete wavelet transform gan for nonhomogeneous dehazing," in 2021 IEEE/CVF Conference on Computer Vision and Pattern Recognition Workshops (CVPRW), 2021, pp. 203–212.
- [15] S.-H. Gao, M.-M. Cheng, K. Zhao, X.-Y. Zhang, M.-H. Yang, and P. Torr, "Res2net: A new multi-scale backbone architecture," *IEEE Transactions on Pattern Analysis and Machine Intelligence*, vol. 43, no. 2, pp. 652–662, 2021.
- [16] H. Zhou, W. Dong, Y. Liu, and J. Chen, "Breaking through the haze: An advanced nonhomogeneous dehazing method based on fast fourier convolution and convnext," in 2023 IEEE/CVF Conference on Computer Vision and Pattern Recognition Workshops (CVPRW), 2023, pp. 1895–1904.
- [17] Z. Liu, H. Mao, C.-Y. Wu, C. Feichtenhofer, T. Darrell, and S. Xie, "A convnet for the 2020s," in 2022 IEEE/CVF Conference

- on Computer Vision and Pattern Recognition (CVPR), 2022, pp. 11966–11976.
- [18] N. Voudoukis, "Inverse square law for light and radiation: A unifying educational approach," *European Journal of Engineering Research and Science*, vol. 2, 11 2017.
- [19] H. Liang, A. Lucian, R. Lange, C. S. Cheung, and B. Su, "Remote spectral imaging with simultaneous extraction of 3d topography for historical wall paintings," *ISPRS Journal of Photogrammetry and Remote Sensing*, vol. 95, pp. 13–22, 2014.
 [20] X. Qin, Z. Wang, Y. Bai, X. Xie, and H. Jia,
- [20] X. Qin, Z. Wang, Y. Bai, X. Xie, and H. Jia, "Ffa-net: Feature fusion attention network for single image dehazing," *Proceedings of the AAAI Conference on Artificial Intelligence*, vol. 34, no. 07, pp. 11908–11915, Apr. 2020.
- [21] L. Chi, B. Jiang, and Y. Mu, "Fast fourier convolution," in *Advances in Neural Information Processing Systems*, H. Larochelle, M. Ranzato, R. Hadsell, M. Balcan, and H. Lin, Eds., vol. 33. Curran Associates, Inc., 2020, pp. 4479–4488.
- [22] B. Huang, Z. Li, C. Yang, F. Sun, and Y. Song, "Single satellite optical imagery dehazing using sar image prior based on conditional generative adversarial networks," in 2020 IEEE Winter Conference on Applications of Computer Vision (WACV), 2020, pp. 1795–1802.
- [23] M. E. Paoletti, J. M. Haut, S. K. Roy, and E. M. T. Hendrix, "Rotation equivariant convolutional neural networks for hyperspectral image classification," *IEEE Access*, vol. 8, pp. 179 575–179 591, 2020.
- [24] U. Sara, M. Akter, and M. S. Uddin, "Image quality assessment through fsim, ssim, mse and psnr—a comparative study," *Journal of Computer and Communications*, vol. 07, pp. 8–18, 01 2019.
- [25] Z. Wang, A. Bovik, H. Sheikh, and E. Simoncelli, "Image quality assessment: from error visibility to structural similarity," *IEEE Transactions on Image Processing*, vol. 13, no. 4, pp. 600–612, 2004.